The Astrophysical Journal, 890:168 (15pp), 2020 February 20 https://doi.org/10.3847/1538-4357/ab6f05

The Gravitational Lensing Signatures of BOSS Voids in the Cosmic Microwave Background

Srinivasan Raghunathan[1], Seshadri Nadathur[2], Blake D. Sherwin[3,4], and Nathan Whitehorn[1]
[1] Department of Physics and Astronomy, University of California, Los Angeles, CA 90095, USA; sri@physics.ucla.edu
[2] Institute of Cosmology and Gravitation, University of Portsmouth, Burnaby Road, Portsmouth PO1 3FX, UK; seshadri.nadathur@port.ac.uk
[3] Kavli Institute for Cosmology, University of Cambridge, Madingley Road, Cambridge CB3 OHA, UK
[4] Department of Applied Mathematics and Theoretical Physics, University of Cambridge, Wilberforce Road, Cambridge CB3 0WA, UK
Received 2019 November 21; revised 2020 January 10; accepted 2020 January 21; published 2020 February 26

Abstract

We report a 5.3σ detection of the gravitational lensing effect of cosmic voids from the Baryon Oscillation Spectroscopic Data Release 12 seen in the *Planck* 2018 cosmic microwave background (CMB) lensing convergence map. To make this detection, we introduce new optimal techniques for void stacking and filtering of the CMB maps, such as binning voids by a combination of their observed galaxy density and size to separate those with distinctive lensing signatures. We calibrate theoretical expectations for the void lensing signal using mock catalogs generated in a suite of 108 full-sky lensing simulations from Takahashi et al. Relative to these templates, we measure the lensing amplitude parameter in the data to be $A_L = 1.10 \pm 0.21$ using a matched-filter stacking technique and confirm it using an alternative Wiener-filtering method. We demonstrate that the result is robust against thermal Sunyaev–Zel'dovich contamination and other sources of systematics. We use the lensing measurements to test the relationship between the matter and galaxy distributions within voids and show that the assumption of linear bias with a value consistent with galaxy clustering results is discrepant with observation at $\sim 3\sigma$; we explain why such a result is consistent with simulations and previous results, and is expected as a consequence of void selection effects. We forecast the potential for void CMB lensing measurements in future data from the Advanced ACT, Simons Observatory, and CMB-S4 experiments, showing that, for the same number of voids, the achievable precision improves by a factor of more than 2 compared to *Planck*.

Unified Astronomy Thesaurus concepts: Cosmology (343); Cosmic microwave background radiation (322); Weak gravitational lensing (1797); Large-scale structure of the universe (902); Voids (1779)

1. Introduction

Although most effort in cosmology has naturally been directed toward an understanding of the bright galaxies and clusters in the high-density peaks of the matter distribution in the universe, the study of their counterparts in the cosmic web —the vast low-density regions known as cosmic voids—has recently gained significant importance for cosmology.

As a consequence of their low matter content, voids become dominated by dark energy at early times, and so are sensitive to its nature (Lee & Park 2009; Bos et al. 2012; Lavaux & Wandelt 2012; Pisani et al. 2015). The dynamics within voids can be accurately modeled by linear perturbation theory even on small scales (Cai et al. 2016; Nadathur & Percival 2019; Nadathur et al. 2019a), which provides a unique opportunity to measure the growth rate of structure through redshift-space distortions (RSDs) in the distribution of galaxies around voids (some examples of these studies in survey data include Hamaus et al. 2016; Achitouv et al. 2017; Hawken et al. 2017; Nadathur et al. 2019b). A recent analysis by Nadathur et al. (2019b) of the redshift-space void–galaxy correlation observed in the Baryon Oscillation Spectroscopic survey (BOSS; Dawson et al. 2013) showed that in combination with galaxy clustering, this method reduces the uncertainty in the measurement of cosmological distance scales by 50% compared to previous results based on baryon acoustic oscillations (Alam et al. 2017). An important ingredient for such studies is knowledge of the dark matter distribution within voids. This cannot be directly observed and so is currently calibrated from simulations but in principle could be inferred from measurement of the stacked gravitational lensing signal from voids (Krause et al. 2013).

The matter distribution within voids is also interesting in its own right, as it has been shown to be sensitive to the sum of neutrino masses (e.g., Massara et al. 2015; Banerjee & Dalal 2016; Kreisch et al. 2019; Zhang et al. 2019) and to alternative theories of gravity (e.g., Barreira et al. 2015; Cai et al. 2015; Baker et al. 2018; Cautun et al. 2018; Falck et al. 2018; Paillas et al. 2019). This latter sensitivity is because voids constitute low-density environments within which the screening mechanisms of some modified gravity models do not apply. Several detections of the void lensing shear signal have been made in different data (Melchior et al. 2014; Clampitt & Jain 2015; Sánchez et al. 2017; Fang et al. 2019).

In addition to their lensing effect, voids also have a gravitational redshifting effect on photons traversing them, imprinting small secondary anisotropies on the cosmic microwave background (CMB) via the integrated Sachs–Wolfe (ISW) effect. An early high-significance observation of the void ISW signal (Granett et al. 2008) was found to be strongly discrepant with predictions for the standard Λ Cold Dark Matter (ΛCDM) cosmological model (Nadathur et al. 2012; Flender et al. 2013). This led to much subsequent work on the cross-correlation of voids with CMB temperature maps in newer data (e.g., Cai et al. 2014; Granett et al. 2015; Hotchkiss et al. 2015; Planck Collaboration et al. 2016d; Nadathur & Crittenden 2016; Kovács et al. 2017, 2019), although conclusions regarding the severity of the discrepancy (if any) differ, and detection significances remain low. Less attention

has been paid to the cross-correlation of voids with CMB lensing convergence maps—although Cai et al. (2017) and recently Vielzeuf et al. (2019) have both reported $\sim 3\sigma$ detections of CMB lensing by voids.

The cross-correlation between maps of the reconstructed CMB lensing convergence κ and other tracers of the low-redshift large-scale structure has been the subject of much recent study (e.g., Schmittfull & Seljak 2018; Ade et al. 2019). CMB lensing has been used to measure masses of dark matter halos (initial detections include Baxter et al. 2015; Madhavacheril et al. 2015; Planck Collaboration et al. 2016b). Its correlation with cosmic filaments was also used to study the nonlinearities in structure formation (He et al. 2018). Chantavat et al. (2016) argued that the measurement of the CMB lensing by voids can be used as a probe of cosmological parameters.

In this work, we use the full-sky reconstructed κ map from the *Planck* 2018 data release (Planck Collaboration et al. 2018a) and over 7000 voids extracted from the CMASS spectroscopic galaxy sample of the BOSS Data Release 12 catalogs to examine the CMB lensing imprint of voids. Our work uses similar data to those used by Cai et al. (2017), who reported a 3.2σ detection of the void κ signal, albeit with a slightly different void catalog and the latest *Planck* lensing reconstruction in place of the 2015 map. However, we introduce new improved methods for void stacking that greatly increase the detection sensitivity (Section 4). We calibrate theoretical expectations for the void lensing signal using mock void catalogs in a suite of 108 full-sky lensing simulations produced by Takahashi et al. (2017) in Section 3. Relative to this expectation, in Section 5 we report measurement of a lensing amplitude of $A_L = 1.10 \pm 0.21$ using an optimal matched-filter technique and $A_L = 0.97 \pm 0.19$ using an alternative Wiener-filtering approach, representing detection of the void CMB lensing signal at significance levels of 5.3σ and 5.1σ, respectively. We demonstrate that this detection is robust against thermal Sunyaev–Zel'dovich (tSZ) contaminations in lensing reconstruction and other systematic effects.

The improved measurement precision of the lensing convergence imprint of voids allows us to test the total matter distribution within these voids and to compare it to the distribution of visible galaxies. In Section 5, we show that the void matter overdensity profile $\delta(r)$ naively inferred from direct measurement of the galaxy density profile $\delta_g(r)$ and the assumption of a constant linear galaxy bias consistent with values obtained from galaxy clustering lead to a predicted lensing imprint that differs sharply from that obtained from calibration with the lensing simulations. This naïve bias model is also seen to be in disagreement with the measured κ signal at $\sim 3\sigma$, predicting a lensing amplitude almost 40% larger than that observed. We discuss why this discrepancy is expected due to selection effects arising from the fact that voids are selected as regions of low galaxy density and show that it is consistent with previous results from simulations and data.

In Section 6, we forecast that the expected sensitivity for similar void lensing measurements improves by a factor of 2 or more using new CMB lensing data from current and next-generation experiments (Henderson et al. 2016; Abazajian et al. 2019; Ade et al. 2019) Finally, we summarize our results in Section 7.

2. Data Sets

2.1. CMB Lensing Maps

We make use of the public CMB lensing convergence maps from the *Planck* 2018 data release (Planck Collaboration et al. 2018a).[5] Our fiducial analysis uses the map `COM_Lensing_4096_R3.00` reconstructed using a minimum-variance (MV) quadratic estimator (Hu & Okamoto 2002) from a combination of foreground-cleaned `SMICA` (Planck Collaboration et al. 2016a) CMB temperature and polarization maps, with the mean field subtracted and a conservative mask applied to galaxy clusters to reduce contamination from tSZ contributions. As tSZ signals are known to be a potential contaminant for the CMB lensing reconstruction (van Engelen et al. 2014; Madhavacheril & Hill 2018), and as Alonso et al. (2018) reported a detection of tSZ within voids, we also test for residual systematics in our measurement using a second convergence map (`COM_Lensing-Szde-proj_4096_R3.00`) reconstructed from tSZ-deprojected `SMICA` temperature data alone.

For both maps, we use information from lensing modes $L \leqslant 2048$. Higher L modes are highly noise dominated for the *Planck* lensing reconstruction and are in any case irrelevant for the void lensing signal of interest here, which varies on degree scales. We tested the use of an additional high-pass filter to restrict the multipole range to $8 \leqslant L \leqslant 2048$ as used by Planck Collaboration et al. (2018a), but found that it made negligible difference to the results obtained. Our default analysis presented below therefore does not exclude the largest scale modes $L < 8$.

2.2. BOSS Data and Void Catalog

To construct the void catalog used, we use the CMASS galaxy sample from the BOSS (Dawson et al. 2013) Data Release 12 galaxy catalogs (Alam et al. 2015), which comprise the final data release of the third generation of the Sloan Digital Sky Survey (SDSS-III; Eisenstein et al. 2011). BOSS measured optical spectra for over 1.5 million targets covering nearly 10,000 deg^2 of the sky. The CMASS sample selection is based on color–magnitude cuts designed to select massive galaxies in a narrow range of stellar mass with redshifts $0.43 \leqslant z \leqslant 0.7$ (Reid et al. 2016). These galaxies are biased tracers of the matter distribution, with a bias of $b_{\rm CMASS} \sim 2$ (Alam et al. 2017). Voids from this CMASS sample have previously been used in a variety of works (e.g., Hamaus et al. 2016; Nadathur 2016; Nadathur & Crittenden 2016; Cai et al. 2017; Nadathur et al. 2019b).

We construct a void catalog from the CMASS data using the public `REVOLVER` void-finding code (Nadathur et al. 2019b, 2019c),[6] which is derived from the earlier `ZOBOV` algorithm (Neyrinck 2008). `REVOLVER` estimates the local galaxy overdensity field from the discrete galaxy distribution using a Voronoi tessellation field estimator (VTFE) technique including additional corrections for the CMASS selection function and the survey angular completeness and masks using appropriate weights, as described in detail in Nadathur & Hotchkiss (2014), Nadathur (2016), and Nadathur et al. (2019b). Locations of minima of this density field are identified as the sites of potential voids, the extents of which are

[5] Downloaded from https://pla.esac.esa.int/#cosmology.
[6] Available from https://github.com/seshnadathur/Revolver.

determined by a watershed algorithm without predetermined assumptions about void shapes. Following previous works (Nadathur & Hotchkiss 2015; Nadathur 2016), we define each individual density basin as a distinct void, so that voids do not overlap. REVOLVER provides an option to remove RSD in the void positions using density-field reconstruction prior to void finding (Nadathur et al. 2019a, 2019b), but this step has a negligibly small effect on the predicted lensing signal of voids, and so is omitted here. Thus, our void-finding procedure matches that previously used by Nadathur & Crittenden (2016).

The resulting catalog contains a total of 7378 voids, with a redshift distribution that is close to flat. Their low central density means that the lensing imprint of voids qualitatively corresponds to a demagnification ($\kappa < 0$) near the void center. The matter distribution around a typical void also shows an overdensity ($\delta > 0$) around the void boundaries, caused by the pileup of matter evacuated from the center. These walls produce a ring feature of $\kappa > 0$ around the central minimum. In this work, void centers are identified as the center of the largest sphere completely empty of galaxies that can be inscribed within the void, which is the best predictor of the location of the matter density minimum (Nadathur & Hotchkiss 2015). A commonly used alternative choice is to define the void center as the weighted average position of the galaxies within it, or barycenter. This latter choice instead emphasizes the high-density void walls and therefore the $\kappa > 0$ ring, while smoothing out or even missing the central minimum. While this shape of the convergence profiles $\kappa(\theta)$ for voids is less intuitive, both dip- and ring-type imprints can be detected in lensing convergence maps, so the choice makes no practical difference to the detection sensitivity.

For each void, we calculate an average galaxy overdensity $\bar{\delta}_g$, defined as the volume-weighted average of the VTFE overdensity values in each of the Voronoi cells comprising the void (Nadathur et al. 2017), and an effective spherical radius r_v, defined as the radius of the sphere with the same volume as the (arbitrarily shaped) void. The nature of the watershed algorithm means that void extents are always defined to include the high-density regions in the separating walls, and as a result, $\bar{\delta}_g$ is typically ~ 0 but can be either positive or negative (see the discussion in Nadathur & Hotchkiss 2015). Void sizes lie in the range $9.4 \leqslant r_v \leqslant 111\ h^{-1}$ Mpc, with a well-defined maximum around the median value $r_v = 41\ h^{-1}$ Mpc. The median void redshift is $z = 0.55$, and the median angular scale subtended by spheres of the same r_v would be $\sim 1\overset{\circ}{.}6$.

From these values, for each void in the catalog, we construct the dimensionless parameter

$$\lambda_v \equiv \bar{\delta}_g \left(\frac{r_v}{1\ h^{-1}\ \mathrm{Mpc}} \right)^{1.2}, \tag{1}$$

which Nadathur et al. (2017) empirically found to be tightly correlated with the void density profiles and large-scale environments. In Sections 3 and 4, we discuss the scaling of the void lensing convergence profiles with λ_v and how this informs our filtering templates.

2.3. Lensing Simulations

The contribution to the CMB lensing convergence profile from an isolated void with a known spherically symmetric matter overdensity distribution $\delta(r)$ can be written as

$$\kappa(\theta) = \frac{3\Omega_m H_0^2}{2c^2} \int \frac{\chi(\chi_s - \chi)}{\chi_s} \frac{\delta(\theta, \chi)}{a} d\chi, \tag{2}$$

where χ is the comoving radial coordinate and χ_s is the comoving distance to the last scattering surface. However, in general, $\delta(r)$ is not known except from calibration with simulations, and voids are not completely isolated, so the effects of other structures along the line of sight need to be accounted for.

To make model predictions for the void lensing signal and to calibrate the optimal filters for application to data, we therefore make use of the public suite of full-sky lensing simulations described by Takahashi et al. (2017).[7] These consist of 108 realizations of full-sky lensing convergence and shear maps for all structures between redshifts $z = 0.05$ and 5.3, constructed from multiple N-body simulations in a flat ΛCDM cosmology run using Gadget2 (Springel 2005), with ray tracing performed using the public GRayTrix (Hamana et al. 2015; Shirasaki et al. 2015) code. For this work, we use the maps corresponding to the source redshift at the surface of last scattering, $z_s = 1100$, labeled zs = 66, in HEALPix (Górski et al. 2005) format. We downsample the simulated maps from $N_{\mathrm{side}} = 4096$ to $N_{\mathrm{side}} = 2048$, corresponding to a pixel angular resolution of $1\overset{\prime}{.}7$.

The cosmological parameters used for these simulations are based on the WMAP9 cosmology (Hinshaw et al. 2013): $\Omega_m = 0.279$, $\Omega_b = 0.046$, $\Omega_\Lambda = 0.721$, $n_s = 0.97$, $h = 0.7$, $\sigma_8 = 0.82$. These values unavoidably differ slightly from the *Planck* best-fit cosmology that is used elsewhere in this paper. We will assume that the effect of this on the calibration of our lensing templates is small and ignore it for the purposes of this work. Note that this is not an unreasonable approximation, as the most relevant parameter for determining the matter content of voids (and thus their lensing convergence κ) is σ_8 (Nadathur et al. 2019b), and for the Takahashi simulations this is quite close to the *Planck* value $\sigma_8 = 0.81$ (Planck Collaboration et al. 2018b).

Halo catalogs on the lightcone are provided with each of these simulations. In the redshift range $0.4 \lesssim z \lesssim 0.75$ of interest to us, the minimum halo mass resolution is $2 \times 10^{12}\ h^{-1} M_\odot$. From these halo catalogs, we create galaxy mocks using the halo occupation distribution model of Zheng et al. (2007), with parameters as specified by Manera et al. (2013) in order to match the clustering properties of CMASS galaxies. We apply the BOSS survey footprint and angular and radial selection functions in order to match the CMASS sample as closely as possible. To each mock catalog, we then apply the same void-finding procedure described in Section 2.2 used for the BOSS data to obtain 108 mock void catalogs, each consisting of $\sim$7000 voids.

2.4. MD-Patchy Mock Void Catalogs

In order to reliably estimate the covariance matrix for the lensing measurements, it is desirable to use as large a sample of mocks as possible. The Takahashi simulations provide only 108 realizations, so we use voids from a suite of 2048 MD-Patchy mock galaxy catalogs created for the BOSS

[7] http://cosmo.phys.hirosaki-u.ac.jp/takahasi/allsky_raytracing/

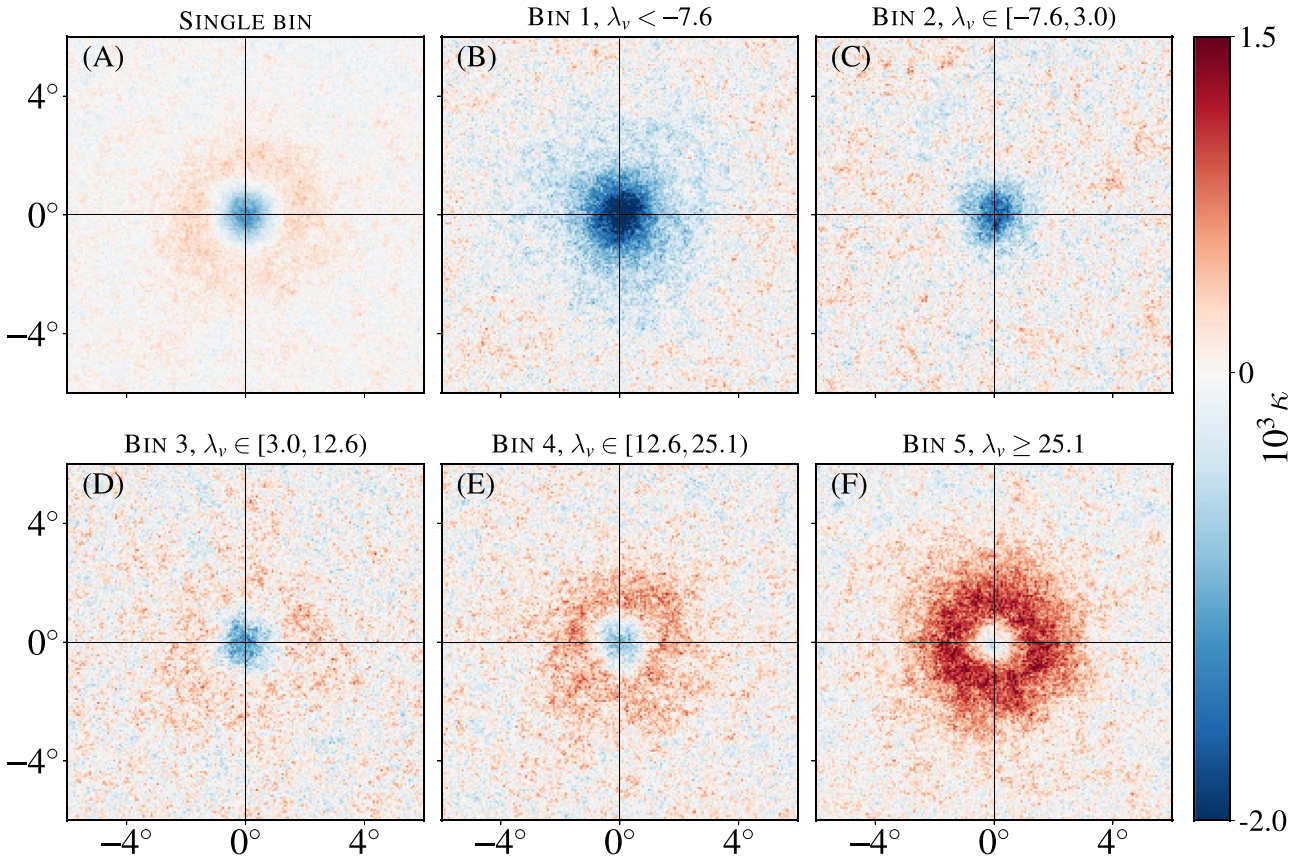

Figure 1. Stacked convergence ($10^3\kappa$) maps at void locations in the Takahashi simulations. Cutouts of size $10^\circ \times 10^\circ$ centered at void positions were extracted from the lensing maps and averaged. Panel (A) shows the resultant stack for all voids in a single bin. Panels (B) through (F) show stacked signals for different subpopulations of voids, binned according to their λ_v values as indicated. Bin boundaries are chosen such that each bin contains roughly 1400 voids in each of the 108 realizations. The predominantly positive κ signal in (F) is a projection effect caused by looking through high-density walls around the voids, which still correspond to genuine matter underdensities at their centers.

DR12 data release (Kitaura et al. 2016) instead.[8] These mocks are created using the fast PATCHY algorithm, based on approximate simulations using augmented Lagrangian perturbation theory (Kitaura & Heß 2013). Mock galaxies are painted in dark matter halos using a halo abundance matching algorithm (Rodríguez-Torres et al. 2016) trained on a reference full *N*-body simulation from the Big MultiDark suite (Klypin et al. 2016). The mocks were designed and validated to match the clustering of the CMASS sample and to reproduce the selection functions and observational systematics. Note that the MD-Patchy mocks are used only for covariance matrix estimation and not template calibration, as they do not have the associated CMB lensing simulations.

We run `REVOLVER` on each of these MD-Patchy mocks in the same way as for the CMASS data sample, thus obtaining 2048 mock void catalogs that statistically closely match the BOSS voids. Similar mock void catalogs have been used for covariance estimation for void measurements by Nadathur & Crittenden (2016), Nadathur et al. (2019b). These MD-Patchy voids have the same clustering properties as the BOSS voids and occupy the same section of the *Planck* sky defined by the BOSS footprint, but are uncorrelated with real structures and thus with the *Planck* κ map. This is expected to be a sufficient approximation for error bar calculation; the CMB lensing and void fields should only have a modest correlation coefficient, so that the correlated cosmic variance contribution to the errors is expected to be negligible.

[8] Alternatively, one could keep the BOSS void catalog fixed and repeat the stacking on the public *Planck* lensing simulations. But only 300 lensing realizations are available, which is also small relative to the size of the covariance matrix to be estimated (Section 4.2).

3. Void Lensing in Simulation

We start by analyzing the void lensing convergence signal seen in the Takahashi simulations from Section 2.3 in order to calibrate theoretical expectations for the void lensing profile $\kappa(\theta)$. Panel (A) in Figure 1 shows the stacked average κ signal around void lines of sight in the simulations, constructed by stacking equal $10^\circ \times 10^\circ$ patches cut out from the full-sky κ maps centered at void positions. This stack contains all the voids from all of the realizations of the simulations and shows qualitative features in accord with intuition: a small central region with $\kappa < 0$, (i.e., a demagnification due to the central void underdensity), surrounded by a larger but less-pronounced positive convergence ring corresponding to the location of the overdensity at the void boundary, caused by the pileup of matter evacuated from the void center.

Several authors (e.g., Hotchkiss et al. 2015; Cai et al. 2017; Kovács et al. 2017, 2019; Vielzeuf et al. 2019) advocate rescaling the angular sizes of each cutout based on the angular

scale corresponding to the individual void radius r_v before stacking. Under the assumption that the angular sizes of the void lensing imprints of interest scale self-similarly with the void radius r_v, such a rescaling procedure would maximize the signal amplitude. However, Nadathur et al. (2017) showed that the shapes of void lensing convergence profiles are much more strongly correlated with the combination of void size and density encapsulated in parameter λ_v defined by Equation (1) than with r_v alone.

We therefore bin the simulation void samples into $N_{\rm bin} = 5$ bins of λ_v and perform the stacking separately in each bin, shown in panels (B) through (F) in Figure 1. The bin boundaries were chosen based on quintiles of the λ_v distribution for the BOSS voids. Each realization of the Takahashi simulations then contains ∼1400 voids in each bin.[9] The void lensing signal shows an extremely strong dependence on λ_v. Negative values of λ_v (bins 1 and 2) correspond to voids embedded within low-density regions, producing $\kappa \leqslant 0$ everywhere. Voids with a large positive λ_v (bin 5) correspond to local minima within larger-scale overdensities, producing a very pronounced $\kappa > 0$ convergence ring. In other words, small (i.e., large negative) values of λ_v correspond to R-type voids (Ceccarelli et al. 2013; Paz et al. 2013; Ruiz et al. 2019) or "voids in voids" (Sheth & van de Weygaert 2004) within larger-scale underdensities, whereas large positive values of λ_v correspond to S-type voids or "voids in clouds," local density minima sitting within a larger-scale overdensity. The mean void sizes in bins 1 to 5 are $\bar{r}_v = 50.5$, 41.3, 39.6, 38.2, and 37.8 h^{-1} Mpc, respectively, but these values do not correspond to the angular scales subtended by the lensing imprints. The advantage of separating voids by λ_v is clear by comparison to panel (A): if voids of different λ_v are stacked together, the resultant κ signal averages out to a value closer to zero and is consequently harder to detect. Note that the stack for voids in bin 5, with the largest λ_v values, shows primarily positive convergence, $\kappa > 0$, as might be expected from an overdensity. However, this is a projection effect caused by looking through the void walls: these voids do still correspond to genuine underdensities in the matter distribution, with on average $\delta \lesssim -0.4$ at their centers (for instance, see the $\delta(r)$ profiles in Figure 6 of Nadathur et al. 2017).

From these stacks, we measure azimuthally averaged 1D convergence profiles $\kappa(\theta)$ for each λ_v bin, shown in Figure 2. Data points represent the mean convergence value averaged over all voids in each λ_v bin over all 108 simulation realizations. Error bars represent the 68% C.L. uncertainty in the mean convergence for voids in an individual realization; this represents the theoretical uncertainty in the mean signal for a CMASS-like void sample. For each λ_v bin, we fit a polynomial function to the data points and use this to define a template profile $\kappa_{\rm template}(\theta;\, \lambda_v)$ for each stack. The curves in Figure 2 correspond to the templates using polynomial fits. Note that these convergence profiles represent the pixel-space void CMB lensing cross-correlation signals.

[9] We chose $N_{\rm bin} = 5$ for convenience. In principle, $N_{\rm bin}$ should be as large as possible provided uncertainties in the template calibration in each bin remain negligible compared to data uncertainties. However, tests for $N_{\rm bin} > 5$ showed no significant improvement in the expected signal-to-noise ratio (S/N) given *Planck* noise levels.

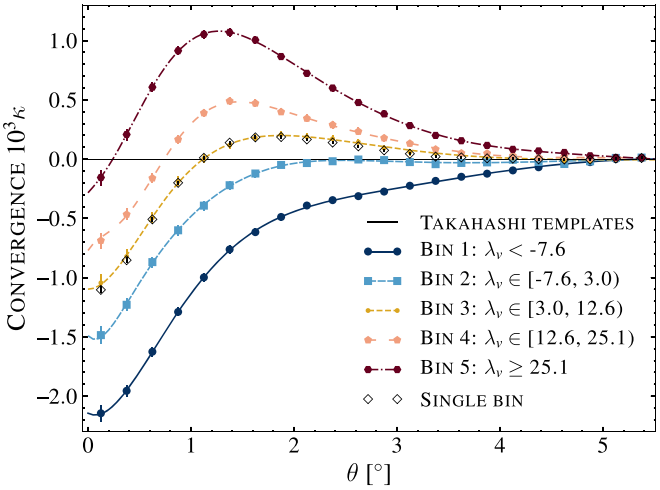

Figure 2. Stacked radial convergence profiles $\kappa(\theta)$ for voids in the Takahashi simulations. Data points show the mean values for voids in the respective bins averaged over all 108 realizations, while error bars indicate the 68% uncertainties in the mean of a single realization containing ∼7000 voids, or ∼1400 in each λ_v bin. The curves are polynomial template fits to the simulation results, which we use to create the matched filters and model the *Planck* data.

4. Methods

4.1. Filtering the Lensing Map

Two significant sources of noise affect the measurement of the void lensing cross-correlation: the lensing reconstruction noise in the *Planck* κ map and the contribution to κ from uncorrelated structures along the line of sight. Both these contributions are orders of magnitude larger than the signal of interest, so the lensing imprint of individual voids is undetectable. This situation is improved by stacking many voids together, especially when the stacks are separated into λ_v bins as discussed in Section 3 above. In addition to this, the application of well-chosen filters to the κ map before stacking can improve the detection sensitivity.

In this work, we follow two different filtering approaches and check that the results obtained from both are in good agreement. The first approach is based on applying a Wiener filter to the *Planck* reconstructed κ map in order to downweight the noise-dominated modes. In spherical harmonic space, the action of the Wiener filter is described by

$$\kappa_{LM}^{\rm WF} = \frac{C_L^{\kappa\kappa}}{C_L^{\kappa\kappa} + N_L^{\kappa\kappa}} \kappa_{LM}, \tag{3}$$

where $C_L^{\kappa\kappa}$ and $N_L^{\kappa\kappa}$ are, respectively, the lensing and noise power spectra for the *Planck* lensing map (Planck Collaboration et al. 2018a). The stacking analysis described below is then performed on patches extracted from this Wiener-filtered map. Note that the design of the Wiener filter in Equation (3) requires knowledge of the lensing reconstruction noise and the overall lensing power for all structures along the line of sight, but does not require knowledge of the expected void lensing imprints of interest obtained from the simulation in the previous section. Thus, by construction, this Wiener filter does not reduce the variance sourced by other structures along the line of sight. This filter could in principle also be modified based on the lensing templates. However, this is already achieved by the optimal matched-filter method described below, and keeping the Wiener

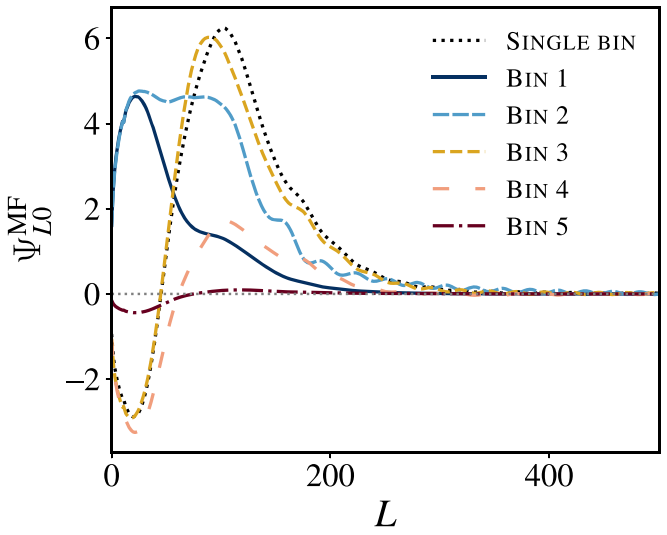

Figure 3. Spherical harmonic coefficients $\Psi^{\rm MF}_{L0}$ for the optimal matched filters designed for the detection of the template lensing profiles in each void λ_v bin, shown in Figure 2. The filters amplify large-scale power and strongly suppress the small scales where voids do not contribute lensing information, with essentially no power at $L > 300$ in any bin.

filtering independent of the simulation templates serves a useful cross-check of that approach.

The second approach we follow is to design optimal matched filters based on the simulation templates obtained in Section 3. To describe the construction of the matched filters, we first represent the total convergence field at a point $\boldsymbol{\theta}$ in the vicinity of the position $\boldsymbol{\theta}_0$ of a void as

$$\kappa(\boldsymbol{\theta}) = \kappa_{\rm template}(|\boldsymbol{\theta} - \boldsymbol{\theta}_0|;\, \lambda_v) + n(\boldsymbol{\theta}), \tag{4}$$

where n represents a generalized noise term that includes all features in the convergence map other than the desired void signal, and $\kappa_{\rm template}$ describes the appropriate void lensing template profile obtained from the Takahashi simulations. We further decompose this template profile as

$$\begin{aligned}\kappa_{\rm template}(\theta;\, \lambda_v) &= \kappa_0(\lambda_v) k(\theta;\, \lambda_v) \\ &= \kappa_0(\lambda_v) \textstyle\sum_{L=0}^{\infty} k_{L0}(\lambda_v) Y^0_L(\cos\theta),\end{aligned} \tag{5}$$

where we have split it into an amplitude term $\kappa_0(\lambda_v) \equiv \kappa_{\rm template}(0;\, \lambda_v)$, and a normalized shape function $k(\theta)$ defined by the spherical harmonic coefficients k_{L0}.

Given this decomposition and the assumption that the noise term is homogeneous and isotropic with zero mean, the spherical harmonic coefficients of the optimal matched filter are uniquely determined (Schäfer et al. 2006; McEwen et al. 2008) to be

$$\Psi^{\rm MF}_{L0}(\lambda_v) = \alpha \frac{k_{L0}(\lambda_v)}{C_L^{N,\rm tot}}, \tag{6}$$

where

$$\alpha^{-1} \equiv \sum_{L=0}^{\infty} \frac{k^2_{L0}(\lambda_v)}{C_L^{N,\rm tot}}, \tag{7}$$

and $C_L^{N,\rm tot} = C_L^{\kappa\kappa} + N_L^{\kappa\kappa}$ is the total power spectrum of the noise field. Figure 3 shows the optimal matched filters in each λ_v bin, designed for the template profiles obtained in Section 3. For comparison, we also show the appropriate matched filter for the stack of all voids together in a single bin as the black dotted line; this is naturally very close to that for the central λ_v bin. Note that the templates corresponding to bin 1 and bin 2 in Figure 2 do not change sign, and therefore the matched filters for these bins do not do so either. For all other bins, a clear crossover point is seen, leading to filter profiles that are partially or fully compensated.

For the matched filter defined in each λ_v bin, the filtered lensing map $\kappa^{\rm MF}$ is a convolution for the filter with the original map,

$$\kappa^{\rm MF}(\boldsymbol{\beta}) = \int d\Omega\, \kappa(\boldsymbol{\theta}) \Psi^{\rm MF}(|\boldsymbol{\theta} - \boldsymbol{\beta}|), \tag{8}$$

which can be written in spherical harmonic space as (Schäfer et al. 2006)

$$\kappa^{\rm MF}_{LM} = \sqrt{\frac{4\pi}{2L+1}}\, \kappa_{LM} \Psi^{\rm MF}_{L0}. \tag{9}$$

The matched-filtered maps for each of the five λ_v bins, together with the Wiener-filtered map, are shown in Figure 4.

The construction of the matched filter ensures that the expectation value of the filtered field at void locations is

$$\langle \kappa^{\rm MF}(0;\, \lambda_v) \rangle = \kappa_0(\lambda_v), \tag{10}$$

meaning that the filter is unbiased, and the variance of the filtered field at this location, $\sigma^2_{\rm MF}(0;\, \lambda_v) = \sum_{L=0}^{\infty} C_L^{N,\rm tot} |\Psi^{\rm MF}_{L0}|^2$, is minimized. The power of the optimal matched filter can be quantified in terms of the maximum detection level (McEwen et al. 2008) for a single isolated void,

$$\Gamma_{1v}(\lambda_v) \equiv \frac{\langle \kappa^{\rm MF}(0;\, \lambda_v) \rangle}{\sigma_{\rm MF}(0;\, \lambda_v)} = \alpha^{-1/2} \kappa_0(\lambda_v). \tag{11}$$

From this we also calculate a related quantity, $\Gamma_{\rm BOSS}$, which is the corresponding maximum detection level for stacks containing as many voids in each bin as are present in the BOSS void catalog. This is calculated by simply dividing the noise by a factor of $\sqrt{N_v}$ and so assumes the void positions are independent of each other and that their profiles do not overlap. It therefore represents an upper bound on the true achievable detection significance. The Γ_{1v} and $\Gamma_{\rm BOSS}$ values obtained are given in Table 1. Comparison with the corresponding values for the stack of all voids together again highlights the advantage of the λ_v-binning strategy employed here. It also shows that the two extreme λ_v bins present by far the most easily detectable lensing signals, as expected from Figures 1 and 2.

4.2. Detecting the Void Lensing Signal

We extract mean-subtracted $10^\circ \times 10^\circ$ patches centered at the location of each void i in the catalog from the Wiener-filtered *Planck* κ map, using which we measure the azimuthally averaged profile $\hat{\kappa}_i^{\rm WF}(\theta)$ in 20 bins of $\Delta\theta = 0.^\circ25$, out to a maximum $\theta_{\rm max} = 5^\circ$. The final Wiener-filtered stacked profile is then obtained as

$$\hat{\kappa}^{\rm WF}(\theta) = \frac{\sum_i w_i \hat{\kappa}_i^{\rm WF}(\theta)}{\sum_i w_i}. \tag{12}$$

This measurement is repeated for voids in each λ_v bin.

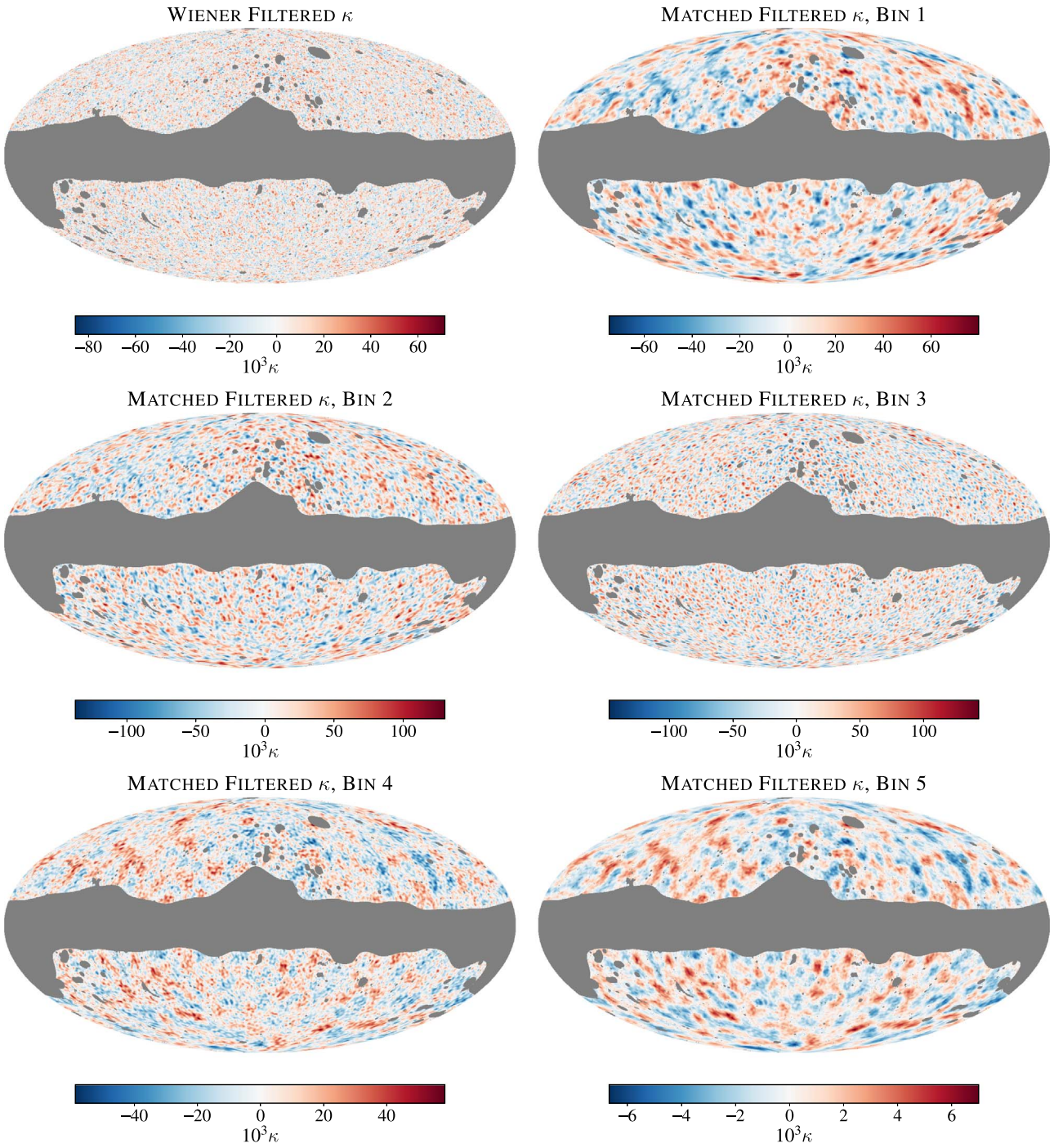

Figure 4. Filtered versions of the *Planck* lensing convergence map. We show the Wiener-filtered map, and the map convolved with each of the optimal matched filters for the λ_v bin templates shown in Figure 3.

Table 1
Expected Maximum Detection Levels under Optimal Matched Filters for a Single Void, and for the BOSS DR12 Void Catalog

Void Stack	λ_v	BOSS N_v	Γ_{1v}	$\Gamma_{\rm BOSS}$
Single bin	[−60.8, 159.8]	7378	0.033	2.80
Bin 1	[−60.8, −7.6)	1478	0.105	4.04
Bin 2	[−7.6, 3.0)	1475	0.047	1.80
Bin 3	[3.0, 12.6)	1473	0.033	1.27
Bin 4	[12.6, 25.1)	1477	0.050	1.91
Bin 5	[25.1, 159.8]	1475	0.110	4.22

The theoretical model to which we compare this observed quantity is

$$\kappa^{\rm th}(\theta) = A_L\,\kappa^{\rm WF}_{\rm template}(\theta), \tag{13}$$

where $\kappa^{\rm WF}_{\rm template}(\theta)$ denotes the template profile for that λ_v bin calibrated from the simulations after convolution with the Wiener filter from Equation (3), and A_L is a free fit parameter representing the lensing amplitude relative to that in the simulation templates.

For the matched-filter analysis, the filter design itself accounts for the lensing profile, so the measured quantity of

interest is only the convergence at the void center location, $\kappa^{\rm MF}(\theta = 0)$. The stacked measurement in this case is

$$\hat{\kappa}^{\rm MF}(0) = \frac{\sum_i w_i[(\hat{\kappa}_i^{\rm MF}(0) - \langle\hat{\kappa}_r^{\rm MF}\rangle]}{\sum_i w_i}. \quad (14)$$

Here, $\langle\hat{\kappa}_r^{\rm MF}\rangle$ is the mean value for the BOSS survey footprint. This is estimated from the mean convergence value in the filtered *Planck* map at the locations of voids in all the MD-Patchy mock catalogs, which cover the same footprint but are uncorrelated with the true lensing signals. This mean subtraction is necessary because the matched-filter design means that the filtered maps shown in Figure 4 contain significant power on scales that are large compared to the sky fraction covered by BOSS (around 23%). The theory model in this case is simply

$$\kappa^{\rm th}(0) = A_L \kappa_0, \quad (15)$$

where as in Equation (13) above we have suppressed the explicit λ_v dependence for simplicity. For the purposes of the current work, we apply a uniform void weighting, $w_i = w = 1$, when calculating both Equations (12) and (14).

The covariance matrix $\hat{\boldsymbol{C}}$ for each measurement above is estimated using the $N_m = 2048$ MD-Patchy mock void catalogs as

$$\hat{\boldsymbol{C}} = \frac{1}{N_m - 1}\sum_{i=1}^{N_m}(\hat{\boldsymbol{\kappa}}_i - \langle\boldsymbol{\kappa}\rangle)(\hat{\boldsymbol{\kappa}}_i - \langle\boldsymbol{\kappa}\rangle)^T. \quad (16)$$

Here, $\hat{\boldsymbol{\kappa}}_i$ is the data vector obtained from repeating the measurement in Equations (12) or (14) using the filtered *Planck* map but with the void catalog obtained from the ith MD-Patchy mock. All λ_v bin measurements are concatenated in the data vector, so that each vector $\hat{\boldsymbol{\kappa}}_i$ has dimensions $p = 5 \times 20 = 100$ for the Wiener-filtered analysis where we measure the profile as a function of θ, and $p = 5$ for the matched-filter case. The covariance matrix therefore has corresponding dimensions 100×100 or 5×5 for the two analyses. For the Wiener-filtered stacking, the covariance matrix has high off-diagonal correlations between radial θ bins.

Given these ingredients, for any value of the model lensing amplitude A_L, we can calculate

$$\chi^2 = \sum_{ij}(\hat{\kappa}_i - \kappa_i^{\rm th})\hat{\boldsymbol{C}}_{ij}^{-1}(\hat{\kappa}_j - \kappa_j^{\rm th}), \quad (17)$$

where the indices i, j run over the $p = 100$ ($p = 5$) dimensions of the data and theory vectors defined by Equations (12) and (13) (Equations (14) and (15)) in the Wiener-filter (matched-filter) analysis. To correctly propagate the uncertainty in the covariance matrix estimation arising from the finite number of mocks used, we use the prescription given by Sellentin & Heavens (2016) and calculate the final likelihood $P(A_L)$ as

$$P(A_L) = \frac{\bar{c}_p|\boldsymbol{C}|^{1/2}}{\left[1 + \frac{\chi^2}{N_m - 1}\right]^{N_m/2}}, \quad (18)$$

where

$$\bar{c}_p = \frac{\Gamma\left(\frac{N_m}{2}\right)}{[\pi(N_m - 1)]^{p/2}\Gamma\left(\frac{N_m - p}{2}\right)}. \quad (19)$$

4.3. Modeling Galaxy Bias within Voids

Measurement of the void lensing signal gives us information on the underlying matter distribution within these regions. It is interesting to compare this to the convergence profile that would be predicted from direct observation of the distribution of visible galaxies, combined with a naive assumption of a constant linear galaxy bias within voids. Denoting the mean galaxy overdensity profile in void regions as $\delta_g(r)$, this assumption allows us to relate it to the mean matter density profile by $\delta_g(r) = b\delta(r)$, where b is the galaxy bias. Generalizing Equation (2) then gives

$$\kappa^{\rm bias}(\theta) = \frac{3\Omega_m H_0^2}{2c^2 b}\int \frac{dn_v(z)}{dz} \times \int \frac{\chi(\chi_s - \chi)}{\chi_s}\frac{\delta_g(\theta, \chi)}{a}d\chi dz, \quad (20)$$

where we have introduced an additional integral over the redshift distribution of the void lenses.

The galaxy overdensity $\delta_g(r)$ is mathematically identical to the monopole of the void–galaxy cross-correlation function, sometimes also denoted as $\xi_0^{vg}(r)$. We measure this monopole as a function of the void–galaxy separation r for each void bin in λ_v using a modified version of the CUTE correlation function code (Alonso 2012)[10] through an implementation of the Landy & Szalay (1993) estimator,

$$\delta_g(r) \equiv \xi_0^{vg}(r) = \frac{D_v D_g(r) - D_v R_g(r) - D_g R_v(r) + R_v R_g(r)}{R_v R_g(r)}. \quad (21)$$

Here, each term $XY(r)$ represents the number of pairs of objects between populations X and Y within the given separation bin, normalized by the total number of pairs, $N_X N_Y$, where N_X is the number of objects in population X. The populations D_v and D_g are the BOSS void and galaxy samples, and R_v and R_g are the corresponding random (unclustered) catalogs of points which match the survey selection function, geometry, and systematic effects present in the data, and contain 50 times as many points as the data. The "galaxy" random catalog R_g is provided with the BOSS public data release. Further details of the construction of the "void" random catalog R_v and the measurement of the cross-correlation are given in Nadathur et al. (2019b).

To convert measurements of $\delta_g(r)$ to model convergence profiles via Equation (20), we assume a value for the bias $b = b_{\rm CMASS} = 2$. This is in line with the mean value of the linear bias deduced from CMASS galaxy clustering measurements (Gil-Marín et al. 2015) and used in BOSS analyses (Alam et al. 2017). This bias model is thus exactly analogous to

[10] The modified code is available from https://github.com/seshnadathur/pyCUTE.

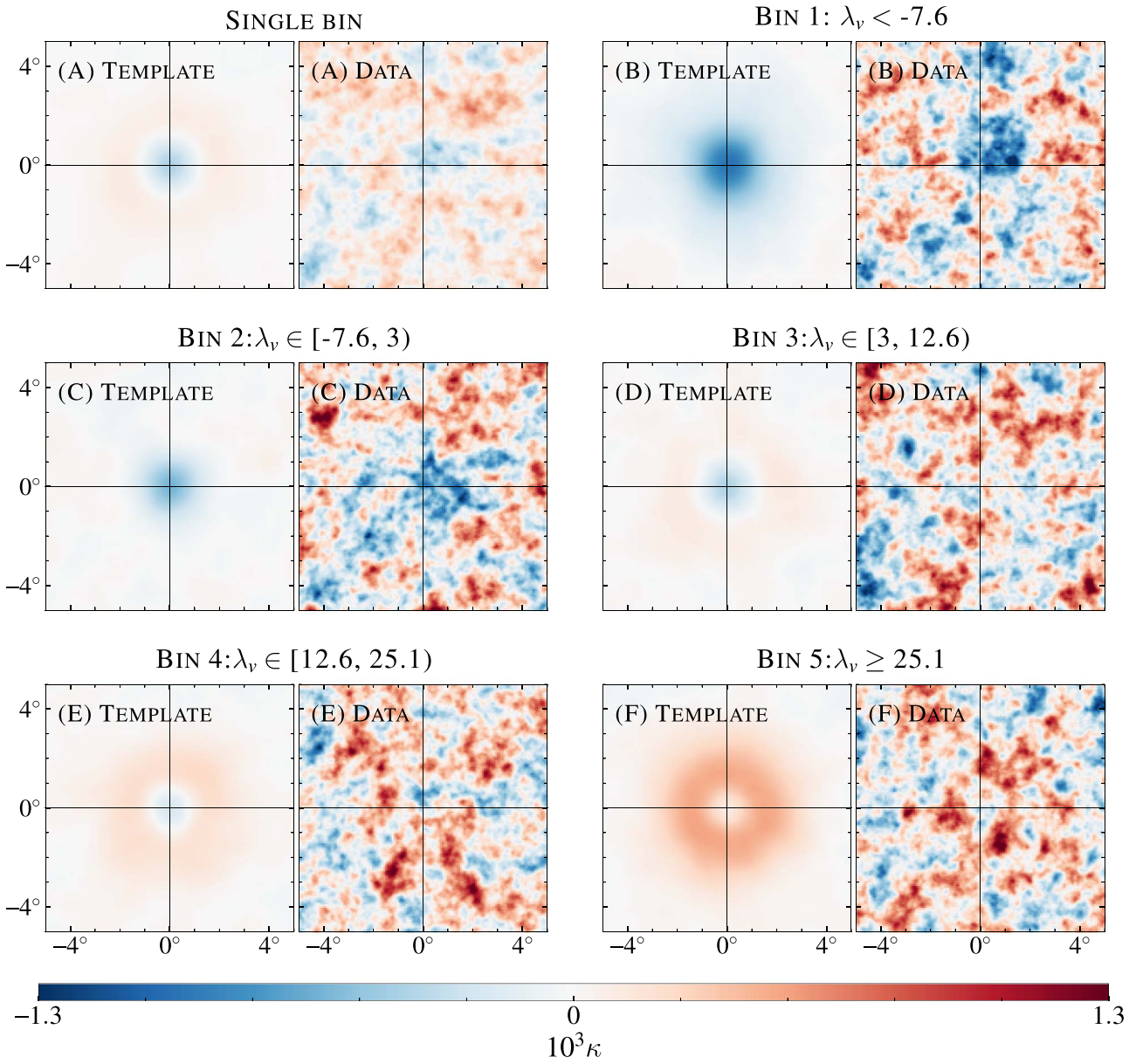

Figure 5. Mean lensing convergence ($10^3\kappa$) signal at the locations of BOSS voids, obtained by stacking patches extracted from the Wiener-filtered *Planck* lensing map. The Wiener-filtered templates (left) and data (right) are shown next to each other to highlight the resemblance between the structures in them. Panel (A) shows the result for the stack of all 7378 voids taken together. Panels (B) through (F) show the stacked results for different subpopulations of voids in bins of increasing λ_v as indicated. Upon comparing panel (A) with others, it is evident that a single bin stack of all voids is suboptimal for the void lensing detection. The positive κ signal in panel (F) is due to the projection effect mentioned in Section 3, combined with the effect of the Wiener filter.

the model used by Alonso et al. (2018) to predict the tSZ signal from voids.

There are many reasons to expect that this naïve assumption might not hold, which include a possible environmental dependence of the bias and a statistical selection bias (Nadathur & Percival 2019) that we discuss further in Section 5.3. Our purpose here is to examine whether the failure of this assumption can be directly seen in the data. To this end, we repeat the fitting procedure described in Section 4.2 using the models of Equation (20) to determine the relative lensing amplitude, denoted $A_L^{\rm naive}$ in this case to distinguish it from that obtained from the simulation template models. The procedure could equivalently be viewed as fitting for the appropriate value of the inverse bias $1/b$.

5. Results

For illustrative purposes, Figure 5 shows the stacked patches extracted from the Wiener-filtered *Planck* κ map at void locations. As in the case of Figure 1, we show the stack for all voids taken together (panel (A)) and for the individual λ_v bins (panels (B) through (F)). We show both the Weiner-filtered templates (left) and the data (right) next to each other to highlight the close resemblance between the structures in the two panels. Even by eye, the $\kappa < 0$ central demagnification region in panel (B) and the $\kappa > 0$ ring in panel (F) are clear. Our quantitative analysis is, however, performed not directly on these stacks but on the azimuthally averaged profiles $\kappa(\theta)$ extracted from them. These are shown in Figure 6, together with the best-fit template profiles in each case. For visual

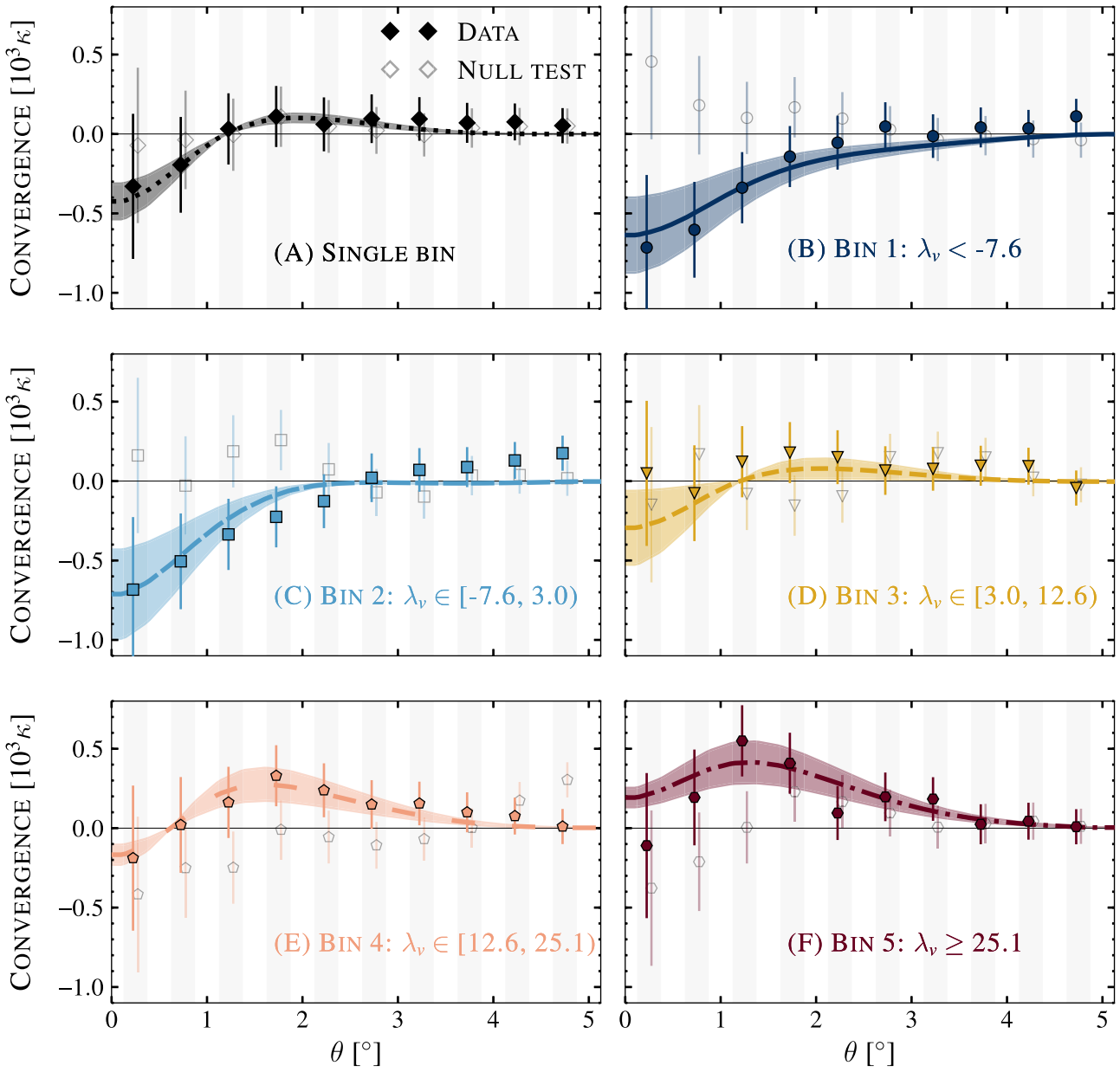

Figure 6. Stacked radial profiles $\hat{\kappa}^{\rm WF}(\theta)$ of the Wiener-filtered CMB lensing convergence around BOSS void center locations shown as filled data points, with error bars derived from the diagonal terms of the covariance matrix. The stacked result for all voids in a single bin is shown in panel (A), with panels (B) through (F) showing stacks in bins of increasing void λ_v. The open data points show null test results obtained from stacks centered at the locations of voids in the mock catalog. The solid curves show the lensing templates from the simulation, after convolution with the Wiener filter and scaled by the best-fit lensing amplitude A_L for each individual bin. The shaded regions indicate the 68% C.L. posterior range for A_L in each case. To avoid visual clutter, data have been rebinned to $\Delta\theta = 0.^\circ5$ from the bin size of $\Delta\theta = 0.^\circ25$ used in fitting. The positive κ signal in panel (F) is due to the projection effect mentioned in Section 3, combined with the effect of the Wiener filter.

clarity, the profiles are shown rebinned into bins of width $\Delta\theta = 0.^\circ5$, though fits are performed with the original binning. Error bars in this figure are derived from the diagonal elements of the covariance matrix, but due to significant off-diagonal contributions, neighboring bins are correlated with each other. For the matched-filter analysis, we plot the observed stack values $\hat{\kappa}^{\rm MF}$ against the model expectations from the templates in Figure 7.

The results obtained for fits to the void lensing amplitude A_L using the two filtering and stacking approaches described in Section 4 are summarized in Figure 8. Our headline results, obtained for the joint fit to voids in all λ_v bins, are $A_L = 0.97 \pm 0.19$ using the Wiener filtering, and $A_L = 1.10 \pm 0.21$ for the matched filters. These results are in excellent agreement with each other and with the expectation $A_L = 1$ for the lensing templates derived from simulation. They represent rejection of the no-lensing hypothesis at the 5.1σ and 5.3σ significance levels, respectively. The consistency between the two filtering approaches demonstrates that the assumption of template profiles used in designing the matched filters does not introduce any significant biases.

In addition to these headline results, we also fit for A_L separately in each individual void bin and for the stack of all voids together in a single bin. These fits to the Wiener-filtered stacks in individual bins are shown as the model curves in Figure 6. To quantify the goodness of fit in each bin, we

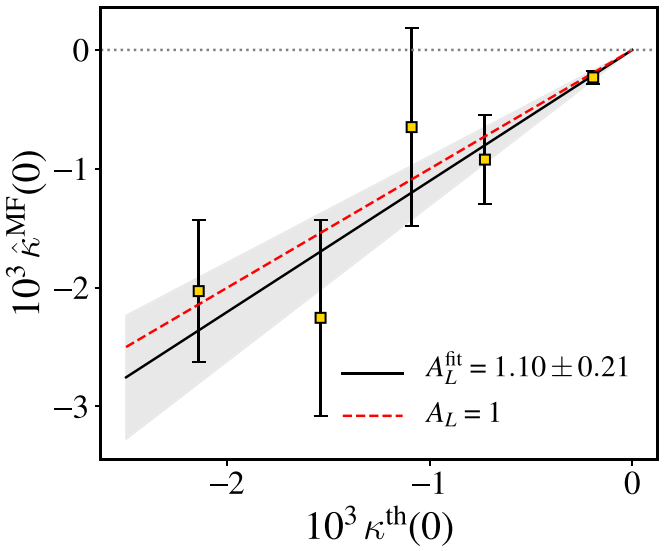

Figure 7. Stacked void lensing contributions $10^3\hat{\kappa}^{\rm MF}(0)$ measured in the matched-filtered *Planck* reconstructed lensing convergence maps in each void λ_v bin, compared to the model values obtained from calibration with lensing simulations as described in the text. Error bars show the square roots of the diagonal entries in the full covariance matrix. Bin values of λ_v increase from left to right. The solid black line shows the best-fit value for the lensing amplitude A_L derived from this data, and the shaded region shows the 68% C.L. posterior range on A_L. The red dashed line shows the fiducial value $A_L = 1$.

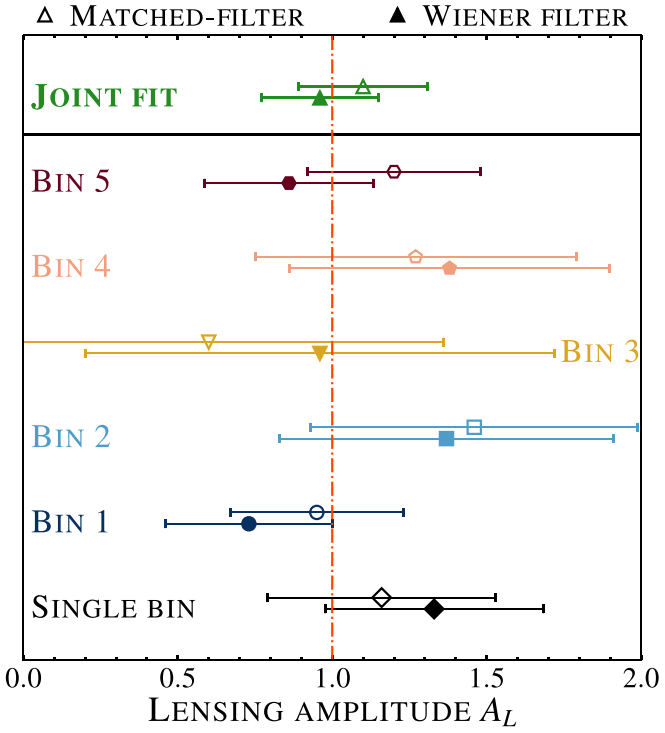

Figure 8. Best-fit amplitudes A_L for the measured void lensing signals relative to the templates from the Takahashi simulations ($A_L = 1$, shown by the red dashed–dotted vertical line). Open and filled points denote the matched-filter and Wiener-filter analyses, respectively. Our headline results, labeled "joint fit," are obtained from jointly fitting for A_L to the measured lensing signal in all five λ_v bins and are shown in the top panel as green triangles. For reference, the results from individual bins and the single-bin stack of all voids together are shown in the bottom panel and are in good agreement with the results in the top panel.

compute the probability-to-exceed values, which are 55%, 69%, 45%, 76%, and 20% for the individual bins; 26% for the single bin all-void stack; and 44% for the combined fit. The A_L fit results are also summarized in Table 2 and Figure 8. In each case, the results obtained are consistent with the combined fit to within the increased statistical errors, showing that there are no significant outliers among the void subpopulations.

5.1. Comparison to Previous Work

Two previous works (Cai et al. 2017; Vielzeuf et al. 2019) have studied the lensing imprints of voids on the CMB, although both report lower significance detections, at just over the 3σ level. Vielzeuf et al. (2019) used a void catalog constructed from the DES Year 1 data. Because these data have only photometric redshifts, the redshift smearing effect favors finding voids in the projected 2D density field rather than the 3D field used here. This leads to preferentially selecting voids that are elongated along the line of sight, and so each void has an enhanced lensing effect compared to those studied here (in this context, see also, e.g., Davies et al. 2018). However, the final void catalog then has a factor of $\sim 6\times$ fewer objects than ours.

In contrast, Cai et al. (2017) use a void catalog that is very similar to ours and is also derived from the BOSS DR12 CMASS sample. Although we do use a later update of the lensed-CMB data, viz. the *Planck* 2018 release rather than the 2015 one, the primary reason for the improved statistical significance reported in this work is our use of the novel stacking strategy recommended by Nadathur et al. (2017), binning voids by the combination of their density and size encapsulated in parameter λ_v. As predicted by Nadathur et al. (2017), we find that the two extreme λ_v bins produce the best detection significance, but that their lensing imprints would partially cancel each other if included in the same stack. The strategy followed by Cai et al. (2017) of instead rescaling lensed-CMB patches in the stack in proportion to the void apparent angular scale is less efficient. Indeed, comparison of the Cai et al. (2017) result with the "single bin" results reported here shows that rescaling on the basis of void size produces only marginally better results than simply stacking all patches together irrespective of void properties. We explicitly checked this by testing an alternative method of rescaling the patches based on the void sizes before stacking without reference to λ_v, as done by Cai et al. (2017), and found a resulting detection significance of $\sim 3.5\sigma$ that closely matches the previous results by those authors and the single-bin results quoted in Table 2.

5.2. Tests for Systematics

We performed a random-positions null test for systematics in our measurement by replacing the BOSS voids used in the data measurement by voids drawn from a randomly selected mock void catalog from the Takahashi simulations. This preserves the effects of the clustering of void positions and their overlap and ensures that patches are drawn from within the same BOSS footprint in the sky (which may be important in the case of inhomogeneous noise properties or large-scale modes affecting the *Planck* κ map). However, the locations in the mock catalog do not have any correlation with the *Planck* CMB lensing and so should return a null signal. The results obtained are shown as open data points in Figure 6 and in Table 2, and are consistent with no lensing signal, as expected.

We then repeated all the measurement and fitting procedures described above for two other cases. First, we checked the

Table 2
Amplitude of Void CMB Lensing Signal Detected in this Work with Respect to the Templates from the Takahashi Simulations, for Different Analysis Choices

Type	Filter	Lensing Amplitude A_L						
		Single Bin	Bin 1	Bin 2	Bin 3	Bin 4	Bin 5	Joint Fit
Baseline	Wiener	1.33 ± 0.35	0.73 ± 0.27	1.37 ± 0.54	0.96 ± 0.76	1.38 ± 0.52	0.86 ± 0.27	0.97 ± 0.19
	Matched	1.16 ± 0.37	0.95 ± 0.28	1.46 ± 0.53	0.60 ± 0.76	1.27 ± 0.52	1.20 ± 0.28	1.10 ± 0.21
tSZ-nulled	Wiener	1.03 ± 0.42	0.73 ± 0.32	0.46 ± 0.62	1.68 ± 0.80	1.47 ± 0.61	0.72 ± 0.32	0.80 ± 0.22
	Matched	0.97 ± 0.44	1.08 ± 0.34	1.14 ± 0.64	1.17 ± 0.89	1.30 ± 0.64	1.23 ± 0.34	1.16 ± 0.34
Null test	Wiener	0.59 ± 0.37	-0.33 ± 0.27	-0.25 ± 0.52	-0.03 ± 0.74	-0.28 ± 0.49	0.31 ± 0.26	0.07 ± 0.19

Note. Our headline results, labeled "joint fit," are obtained from jointly fitting for A_L to the measured lensing signal in all five λ_v bins.

robustness of the results from the Wiener and matched-filter analysis by eliminating both filters; second, we performed a more conservative analysis to check the effect of removing large-scale modes $L < 8$ from the *Planck* κ map. The results obtained for these cases are

$$\begin{aligned} A_L &= 0.98 \pm 0.20 \ (L \leqslant 2048, \text{ no filter}) \\ &= 1.01 \pm 0.19 \ (8 \leqslant L \leqslant 2048, \text{ Wiener filter}) \\ &= 1.17 \pm 0.21 \ (8 \leqslant L \leqslant 2048, \text{ matched-filter}). \end{aligned} \tag{22}$$

These numbers are entirely consistent with the headline results obtained above, indicating no significant contamination from the inclusion of the large-scale modes or the filters used. We also note that, for the current noise levels, the constraints on A_L obtained from the Wiener or matched filters are not significantly better than the result without any filtering. However, the optimal filters used here will be important for measurements with the next-generation low-noise CMB data sets.

As mentioned in Section 2, an important potential contaminant of the void lensing signal comes from tSZ signals. Alonso et al. (2018) already reported a 3.4σ detection cross-correlation of BOSS voids with tSZ signal from a stacking analysis using *Planck* Compton-y maps (Hurier et al. 2013; Planck Collaboration et al. 2016c). The tSZ signal is a known contaminant of the lensing convergence reconstruction from CMB temperature data (van Engelen et al. 2014; Madhavacheril & Hill 2018). We therefore repeated our entire analysis pipeline on the *Planck* convergence map reconstructed from tSZ-deprojected temperature data only. This map produced from the tSZ-nulled CMB map is noisier than the fiducial lensing map produced using an MV combination of data from multiple channels and as a result the detection sensitivity expected is lower than the fiducial case. The resulting A_L constraints are included in Table 2, with final combined fit values

$$\begin{aligned} A_L &= 0.80 \pm 0.22 \ (\text{Wiener filter}) \\ &= 1.16 \pm 0.34 \ (\text{matched-filter}). \end{aligned} \tag{23}$$

These have a higher uncertainty as expected, but are entirely consistent both with our headline results and with $A_L = 1$, indicating no significant tSZ contamination.

We do not directly test for contamination from the kinematic SZ signal arising due to the motion of galaxies (Ferraro & Hill 2018), but given the absence of tSZ contamination, this effect is also expected to be negligible. Finally, we also ignore the possibility of contamination from cosmic infrared background (CIB) emission (Osborne et al. 2014; van Engelen et al. 2014; Schaan & Ferraro 2019), because the CIB is sourced primarily by high-redshift galaxies at $z \geqslant 2$, which should have only a small correlation with the BOSS galaxies at redshifts $z \lesssim 0.7$.

5.3. Testing the Linear Bias Model in Voids

The results above demonstrate that the void CMB lensing signal is seen at high significance and is completely consistent with templates calibrated from the lensing simulations of Takahashi et al. (2017). We now replace these simulation templates with those constructed in Section 4.3 by naively assuming that a constant linear galaxy bias $b = b_{\rm CMASS} = 2$ (Gil-Marín et al. 2015; Alam et al. 2017) is valid within voids. With the exception of the change of templates, the fitting procedure remains the same, although for simplicity in this case we only perform the Wiener-filtered stacking. To avoid confusion, we denote the lensing amplitude measured in this case as $A_L^{\rm naive}$. The result obtained from the joint fit to all bins is

$$A_L^{\rm naive} = 0.64 \pm 0.13. \tag{24}$$

Once again, the results from fits in individual λ_v bins are entirely consistent with the joint result with larger uncertainties, but are not shown explicitly for simplicity.

This value is discrepant with the expectation $A_L = 1$ at 2.8σ, indicating that the observed lensing effect of voids is significantly smaller than would be expected from the assumption of constant linear galaxy bias within voids matching that of the overall CMASS sample. This result can be rephrased in terms of a constraint on the effective bias $b_{\rm eff} = \delta_g/\delta$ within voids: if this constant proportionality held for all r and for all voids, the implied value of the bias would be $b_{\rm eff}^{-1} = 0.32 \pm 0.06$, equivalent to a mean galaxy bias of $b_{\rm eff} = 3.22$ and inconsistent with the results from galaxy clustering at the same $\sim 3\sigma$ level.

These results are consistent with those of Nadathur & Percival (2019), who show that in simulations, the galaxy distribution and matter distribution in voids are not in general related by a simple linear bias relationship and that assuming such a relationship leads to an overestimate of the matter deficit within voids. Our results are also consistent with previous work on the tSZ emission profiles of BOSS voids by Alonso et al. (2018). These authors built a theory model for the tSZ signal assuming linear bias, in a manner entirely analogous to our method in Section 4.3. On fitting the model to data, they find a relative amplitude factor $\alpha_v = 0.67 \pm 0.2$, close to 2σ smaller than the expectation $\alpha_v = 1$, and entirely consistent with our result for $A_L^{\rm naive}$ given their larger uncertainties. Using lensing

shear measurements for a different catalog of voids obtained from galaxy samples in DES Year 1 with photometric redshifts only, Fang et al. (2019) report better agreement with the assumption of a linear relationship between the void matter and galaxy density profiles, but again with an effective bias factor that is in excess of that determined from galaxy clustering for the vast majority (∼85%) of voids (e.g., see their Figure 14).

Contributions to this apparent lack of matter deficit within voids could come from several sources, including the possibility that the relationship between mass and luminous galaxies is fundamentally different in low-density environments. However, as pointed out by Nadathur & Percival (2019), the single biggest contribution is likely to be from a simple statistical effect. Irrespective of the true mean relationship between mass and galaxies in low-density environments, there will necessarily be significant scatter around this mean due to shot noise fluctuations in the galaxy distribution. The fact that voids are selected on the basis of searching for regions of low galaxy density then necessarily introduces a statistical bias in the observed mass-to-light ratio in these selected regions, which works in the direction of these voids containing smaller matter deficits than predicted from their galaxy content. In simulations, this effect leads to deviations of up to ∼25% from the expected $\delta(r)$ (Nadathur & Percival 2019). The only way to completely eliminate this selection bias is to define voids not on the basis of the observed galaxy density field, but directly from the matter density δ. This might be possible by adapting void-finding algorithms to operate on lensing convergence maps rather than the galaxy field, but we leave this to future work.

6. Void CMB Lensing Measurements with Future Data

In this work, we used only lensing reconstruction results from *Planck*. However, future CMB data from Advanced ACT (AdvACT; Henderson et al. 2016), CMB Stage IV (CMB-S4; Abazajian et al. 2019), and Simons Observatory (SO; Ade et al. 2019) are expected to lower the lensing reconstruction noise by an order of magnitude. The noise in the polarization channels of these experiments will also be low enough to allow efficient lensing reconstruction from CMB polarization-only data, eliminating lensing systematics induced by SZ contamination (Hall & Challinor 2014; Yasini & Pierpaoli 2016) and emissions from extragalactic foregrounds that are largely unpolarized (Datta et al. 2019; Gupta et al. 2019), that affect temperature-based CMB lensing maps. These surveys will not be full sky, but will scan roughly 40% of the southern sky, giving sufficient overlap for excellent synergies with optical surveys including DES (Dark Energy Survey Collaboration et al. 2016), the Dark Energy Spectroscopic Instrument (DESI; DESI Collaboration et al. 2016), Euclid (Refregier et al. 2010), and the Large Synoptic Survey Telescope (LSST; LSST Science Collaboration et al. 2009)

In this section, we forecast the detection sensitivity achievable for the void CMB lensing measurement for current "third-generation" and future (CMB-S4 and SO) experiments. To allow an easy comparison to the results from *Planck*, in making these forecasts we assume that the void population used for such a detection has the same properties as the BOSS voids used in the current work. That is, we assume the number of void lenses available for the measurement is fixed, and that their matter profiles and redshift distribution are close enough to those of BOSS voids that their predicted lensing contributions will be similar. We assume a noise level of $\Delta_T = 7.0\ \mu\mathrm{K}'$ ($\Delta_P = \sqrt{2}\,\Delta_T$) for the third-generation experiment and $\Delta_T = 2.0$, 10.0, and 6.3 $\mu\mathrm{K}'$ for CMB-S4, SO-baseline, and SO-goal, respectively. A common beam of 1.′5 at 150 GHz was assumed for all experiments, which corresponds to a telescope with a primary dish size of 6 m. The expected lensing noise curves were computed for the above experiments assuming a maximum lensing multipole $L_{\rm max} = 3000$ for the third-generation experiment and $L_{\rm max} = 4000$ for other experiments. A higher $L_{\rm max}$ was assumed for the next-generation experiments as they are being designed to have a broader frequency coverage compared to current experiments for an efficient suppression of extragalactic foreground signals. We obtained the lensing curves for the temperature-only (TT), MV combination of all the five temperature and polarization-based lensing estimators (TT, TE, EE, EB, and TB), and MV combination of the two polarization-only (MVpol) estimators.

Table 3
Expected S/N of BOSS Voids Using Different CMB Lensing Estimators for Future CMB Surveys

Experiment	Δ_T (μK′)	$L_{\rm max}$	Void Lensing S/N		
			MV	TT	MVpol
Third generation	7.0	3000	9.3	7.5	8.2
CMB-S4	2.0	4000	10.7	9.5	10.1
SO-baseline	10.0	4000	9.4	8.4	8.0
SO-goal	6.3	4000	9.7	9.0	9.1

The forecast achievable S/Ns for the void lensing measurements in these data are summarized in Table 3. All future experiments can reach detection sensitivities far in excess of those achieved with *Planck*, exceeding 10σ for CMB-S4. The lensing S/N from polarization-only channels is equal to or better than the temperature-based estimation for experiments with $\Delta_T \leqslant 7.0\ \mu\mathrm{K}'$. These forecasts can be regarded as conservative because, given the capabilities of surveys such as DESI, Euclid, and LSST, the number of voids used for future measurements is expected to increase.

7. Conclusion

We have reported a high-significance detection, at the 5.3σ level, of the gravitational lensing effect in *Planck* data of cosmic voids found in the BOSS CMASS galaxy sample. The measured signal amplitude and shape are consistent with the lensing templates we derived from mock void catalogs and full-sky CMB lensing maps in a suite of 108 simulations created by Takahashi et al. (2017). We tested our measurement pipeline with two theoretically motivated filtering strategies to reduce the noise in the *Planck* κ map, using optimal matched filters and a Wiener filter, and obtained consistent results with both. The matched-filter technique is designed to maximize the lensing S/N, but the filter design assumes detailed knowledge of the void lensing template, which the Wiener-filter approach does not. The consistency of the two methods therefore serves as a good cross-check that the shape of the lensing signal in the data indeed matches the simulation well. The S/N we report for the void CMB lensing detection here is significantly higher than that reported in two previous studies (Cai et al. 2017; Vielzeuf et al. 2019). This difference is primarily due to

improvements in the stacking methodology introduced here, as well as to improvements in the data sets and filtering.

Our improved sensitivity allows us to probe the relationship between the matter, $\delta(r)$, and galaxy, $\delta_g(r)$, density profiles around void locations. Using direct measurement of the void $\delta_g(r)$ from the galaxy data, we tested the hypothesis that this relationship is linear, with the same constant bias as determined from galaxy clustering analyses of the CMASS sample, and rule it out at $\sim 3\sigma$ significance. This hypothesis overpredicts the amplitude of the void lensing effect by close to 40%; equivalently, if the galaxy bias relationship within voids is truly linear, this bias must be $\sim$60% larger than the value $b_{\rm CMASS} = 2$ deduced from galaxy clustering. This result is not unexpected due to a strong statistical selection bias arising from the void identification that has been confirmed in simulations (Nadathur & Percival 2019), potentially in combination with the impact of additional nonlinear biasing. It is also consistent with the result obtained (albeit with lower significance) in the context of the void–tSZ cross-correlation by Alonso et al. (2018), who also used voids in the CMASS sample. While the linear bias model predictions fail, the predicted lensing profiles obtained from directly tracing the total matter content of voids in simulation is in very good agreement with observation.

Finally, we forecast the S/N achievable for void CMB lensing measurements with future data from current and next-generation experiments like CMB-S4 and SO. These data will allow the detection of the void lensing signal at significance far exceeding that achieved with *Planck*, and with negligible systematics. The precision obtained from these measurements of $\kappa(\theta)$ will then enable inversion to determine the matter profiles $\delta(r)$ directly from data. This method could then replace the current necessity of calibrating these profiles against simulation results for use in other measurement of void dynamics (e.g., Nadathur et al. 2019b). The direct determination of $\delta(r)$ will also be an important factor in the use of voids in cosmological applications, such as probing the sum of neutrino masses Σm_ν and testing modified gravity models.

We thank the anonymous referee for useful suggestions and comments. We thank Ryuichi Takahashi for correspondence regarding the Takahashi et al. (2017) simulations. We acknowledge the Centro de Ciencias de Benasque Pedro Pasqual and the organizers of the workshop "Understanding Cosmological Observations" in 2019 July, where this work was started. S.R. and N.W. acknowledge support from NSF grants AST-1716965 and CSSI-1835865. S.N. is supported by UK Space Agency grant ST/N00180X/1. B.D.S. acknowledges support from an STFC Ernest Rutherford Fellowship, an Isaac Newton Trust Early Career Grant, and from the European Research Council (ERC) under the European Union's Horizon 2020 research and innovation programme (grant agreement No. 851274). This work has made use of the `Hoffmann2` cluster at UCLA and the UK SCIAMA High Performance Computing cluster supported by the ICG, SEPNet, and the University of Portsmouth.

This work has made use of public data from the SDSS-III collaboration. Funding for SDSS-III has been provided by the Alfred P. Sloan Foundation, the Participating Institutions, the National Science Foundation, and the U.S. Department of Energy Office of Science. The SDSS-III website is http://www.sdss3.org/. SDSS-III is managed by the Astrophysical Research Consortium for the Participating Institutions of the SDSS-III Collaboration including the University of Arizona, the Brazilian Participation Group, Brookhaven National Laboratory, Carnegie Mellon University, University of Florida, the French Participation Group, the German Participation Group, Harvard University, the Instituto de Astrofisica de Canarias, the Michigan State/Notre Dame/JINA Participation Group, Johns Hopkins University, Lawrence Berkeley National Laboratory, Max Planck Institute for Astrophysics, Max Planck Institute for Extraterrestrial Physics, New Mexico State University, New York University, Ohio State University, Pennsylvania State University, University of Portsmouth, Princeton University, the Spanish Participation Group, University of Tokyo, University of Utah, Vanderbilt University, University of Virginia, University of Washington, and Yale University.

ORCID iDs

Srinivasan Raghunathan https://orcid.org/0000-0003-1405-378X
Seshadri Nadathur https://orcid.org/0000-0001-9070-3102

References

Abazajian, K., Addison, G., Adshead, P., et al. 2019, arXiv:1907.04473
Achitouv, I., Blake, C., Carter, P., Koda, J., & Beutler, F. 2017, PhRvD, 95, 083502
Ade, P., Aguirre, J., Ahmed, Z., et al. 2019, JCAP, 2019, 056
Alam, S., Albareti, F. D., Allende Prieto, C., et al. 2015, ApJS, 219, 12
Alam, S., Ata, M., Bailey, S., et al. 2017, MNRAS, 470, 2617
Alonso, D. 2012, arXiv:1210.1833
Alonso, D., Hill, J. C., Hložek, R., & Spergel, D. N. 2018, PhRvD, 97, 063514
Baker, T., Clampitt, J., Jain, B., & Trodden, M. 2018, PhRvD, 98, 023511
Banerjee, A., & Dalal, N. 2016, JCAP, 2016, 015
Barreira, A., Cautun, M., Li, B., Baugh, C. M., & Pascoli, S. 2015, JCAP, 8, 028
Baxter, E. J., Keisler, R., Dodelson, S., et al. 2015, ApJ, 806, 247
Bos, E. G. P., van de Weygaert, R., Dolag, K., & Pettorino, V. 2012, MNRAS, 426, 440
Cai, Y.-C., Neyrinck, M., Mao, Q., et al. 2017, MNRAS, 466, 3364
Cai, Y.-C., Neyrinck, M. C., Szapudi, I., Cole, S., & Frenk, C. S. 2014, ApJ, 786, 110
Cai, Y.-C., Padilla, N., & Li, B. 2015, MNRAS, 451, 1036
Cai, Y.-C., Taylor, A., Peacock, J. A., & Padilla, N. 2016, MNRAS, 462, 2465
Cautun, M., Paillas, E., Cai, Y.-C., et al. 2018, MNRAS, 476, 3195
Ceccarelli, L., Paz, D., Lares, M., Padilla, N., & Lambas, D. G. 2013, MNRAS, 434, 1435
Chantavat, T., Sawangwit, U., Sutter, P. M., & Wandelt, B. D. 2016, PhRvD, 93, 043523
Clampitt, J., & Jain, B. 2015, MNRAS, 454, 3357
Dark Energy Survey Collaboration, Abbott, T., Abdalla, F. B., et al. 2016, MNRAS, 460, 1270
Datta, R., Aiola, S., Choi, S. K., et al. 2019, MNRAS, 486, 5239
Davies, C. T., Cautun, M., & Li, B. 2018, MNRAS, 480, L101
Dawson, K. S., Schlegel, D. J., Ahn, C. P., et al. 2013, AJ, 145, 10
DESI Collaboration, Aghamousa, A., Aguilar, J., et al. 2016, arXiv:1611.00036
Eisenstein, D. J., Weinberg, D. H., Agol, E., et al. 2011, AJ, 142, 72
Falck, B., Koyama, K., Zhao, G.-B., & Cautun, M. 2018, MNRAS, 475, 3262
Fang, Y., Hamaus, N., Jain, B., et al. 2019, MNRAS, 490, 3573
Ferraro, S., & Hill, J. C. 2018, PhRvD, 97, 023512
Flender, S., Hotchkiss, S., & Nadathur, S. 2013, JCAP, 1302, 013
Gil-Marín, H., Noreña, J., Verde, L., et al. 2015, MNRAS, 451, 539
Górski, K. M., Hivon, E., Banday, A. J., et al. 2005, ApJ, 622, 759
Granett, B. R., Kovács, A., & Hawken, A. J. 2015, MNRAS, 454, 2804
Granett, B. R., Neyrinck, M. C., & Szapudi, I. 2008, ApJL, 683, L99
Gupta, N., Reichardt, C. L., Ade, P. A. R., et al. 2019, MNRAS, 490, 5712
Hall, A., & Challinor, A. 2014, PhRvD, 90, 063518
Hamana, T., Sakurai, J., Koike, M., & Miller, L. 2015, PASJ, 67, 34
Hamaus, N., Pisani, A., Sutter, P. M., et al. 2016, PhRvL, 117, 091302
Hawken, A. J., Granett, B. R., Iovino, A., et al. 2017, A&A, 607, A54
He, S., Alam, S., Ferraro, S., Chen, Y.-C., & Ho, S. 2018, NatAs, 2, 401
Henderson, S. W., Allison, R., Austermann, J., et al. 2016, JLTP, 184, 772
Hinshaw, G., Larsen, D., Komatsu, E., et al. 2013, ApJS, 208, 19

Hotchkiss, S., Nadathur, S., Gottlöber, S., et al. 2015, MNRAS, 446, 1321
Hu, W., & Okamoto, T. 2002, ApJ, 574, 566
Hurier, G., Macías-Pérez, J. F., & Hildebrandt, S. 2013, A&A, 558, A118
Kitaura, F.-S., & Heß, S. 2013, MNRAS, 435, L78
Kitaura, F.-S., Rodríguez-Torres, S., Chuang, C.-H., et al. 2016, MNRAS, 456, 4156
Klypin, A., Yepes, G., Gottlöber, S., Prada, F., & Heß, S. 2016, MNRAS, 457, 4340
Kovács, A., Sánchez, C., García-Bellido, J., et al. 2017, MNRAS, 465, 4166
Kovács, A., Sánchez, C., García-Bellido, J., et al. 2019, MNRAS, 484, 5267
Krause, E., Chang, T.-C., Doré, O., & Umetsu, K. 2013, ApJL, 762, L20
Kreisch, C. D., Pisani, A., Carbone, C., et al. 2019, MNRAS, 488, 4413
Landy, S. D., & Szalay, A. S. 1993, ApJ, 412, 64
Lavaux, G., & Wandelt, B. D. 2012, ApJ, 754, 109
Lee, J., & Park, D. 2009, ApJL, 696, L10
LSST Science Collaboration, Abell, P. A., Allison, J., et al. 2009, arXiv:0912.0201
Madhavacheril, M., Sehgal, N., Allison, R., et al. 2015, PhRvL, 114, 151302
Madhavacheril, M. S., & Hill, J. C. 2018, PhRvD, 98, 023534
Manera, M., Scoccimarro, R., Percival, W. J., et al. 2013, MNRAS, 428, 1036
Massara, E., Villaescusa-Navarro, F., Viel, M., & Sutter, P. M. 2015, JCAP, 2015, 018
McEwen, J. D., Hobson, M. P., & Lasenby, A. N. 2008, ITSP, 56, 3813
Melchior, P., Sutter, P. M., Sheldon, E. S., Krause, E., & Wandelt, B. D. 2014, MNRAS, 440, 2922
Nadathur, S. 2016, MNRAS, 461, 358
Nadathur, S., Carter, P., & Percival, W. J. 2019a, MNRAS, 482, 2459
Nadathur, S., Carter, P. M., Percival, W. J., Winther, H. A., & Bautista, J. E. 2019b, PhRvD, 100, 023504
Nadathur, S., Carter, P. M., Percival, W. J., Winther, H. A., & Bautista, J. E. 2019c, REVOLVER: REal-space VOid Locations from suVEy Reconstruction, Astrophysics Source Code Library, ascl:1907.023
Nadathur, S., & Crittenden, R. 2016, ApJL, 830, L19
Nadathur, S., & Hotchkiss, S. 2014, MNRAS, 440, 1248
Nadathur, S., & Hotchkiss, S. 2015, MNRAS, 454, 2228
Nadathur, S., Hotchkiss, S., & Crittenden, R. 2017, MNRAS, 467, 4067
Nadathur, S., Hotchkiss, S., & Sarkar, S. 2012, JCAP, 1206, 042
Nadathur, S., & Percival, W. J. 2019, MNRAS, 483, 3472
Neyrinck, M. C. 2008, MNRAS, 386, 2101
Osborne, S. J., Hanson, D., & Doré, O. 2014, JCAP, 2014, 024
Paillas, E., Cautun, M., Li, B., et al. 2019, MNRAS, 484, 1149
Paz, D., Lares, M., Ceccarelli, L., Padilla, N., & Lambas, D. G. 2013, MNRAS, 436, 3480
Pisani, A., Sutter, P. M., Hamaus, N., et al. 2015, PhRvD, 92, 083531
Planck Collaboration, Adam, R., Ade, P. A. R., et al. 2016a, A&A, 594, A9
Planck Collaboration, Ade, P. A. R., Aghanim, N., et al. 2016b, A&A, 594, A24
Planck Collaboration, Ade, P. A. R., Aghanim, N., et al. 2016d, A&A, 594, A21
Planck Collaboration, Aghanim, N., Akrami, Y., et al. 2018a, arXiv:1807.06210
Planck Collaboration, Aghanim, N., Akrami, Y., et al. 2018b, arXiv:1807.06209
Planck Collaboration, Aghanim, N., Arnaud, M., et al. 2016c, A&A, 594, A22
Refregier, A., Amara, A., Kitching, T. D., et al. 2010, arXiv:1001.0061
Reid, B., Ho, S., Padmanabhan, N., et al. 2016, MNRAS, 455, 1553
Rodríguez-Torres, S. A., Chuang, C.-H., Prada, F., et al. 2016, MNRAS, 460, 1173
Ruiz, A. N., Alfaro, I. G., & Garcia Lambas, D. 2019, MNRAS, 483, 4070
Sánchez, C., Clampitt, J., Kovacs, A., et al. 2017, MNRAS, 465, 746
Schaan, E., & Ferraro, S. 2019, PhRvL, 122, 181301
Schäfer, B. M., Pfrommer, C., Hell, R. M., & Bartelmann, M. 2006, MNRAS, 370, 1713
Schmittfull, M., & Seljak, U. 2018, PhRvD, 97, 123540
Sellentin, E., & Heavens, A. F. 2016, MNRAS, 456, L132
Sheth, R. K., & van de Weygaert, R. 2004, MNRAS, 350, 517
Shirasaki, M., Hamana, T., & Yoshida, N. 2015, MNRAS, 453, 3043
Springel, V. 2005, MNRAS, 364, 1105
Takahashi, R., Hamana, T., Shirasaki, M., et al. 2017, ApJ, 850, 24
van Engelen, A., Bhattacharya, S., Sehgal, N., et al. 2014, ApJ, 786, 13
Vielzeuf, P., Kovács, A., Demirbozan, U., et al. 2019, arXiv:1911.02951
Yasini, S., & Pierpaoli, E. 2016, PhRvD, 94, 023513
Zhang, G., Li, Z., Liu, J., et al. 2019, arXiv:1910.07553
Zheng, Z., Coil, A. L., & Zehavi, I. 2007, ApJ, 667, 760